Bimodal Grain Microstructure Development during Hot Compression of a Cast-Homogenized Mg-Zn-Zr Alloy

A. Hadadzadeh, F. Mokdad, B. Shalchi Amirkhiz, M.A. Wells, B.W. Williams, D.L. Chen

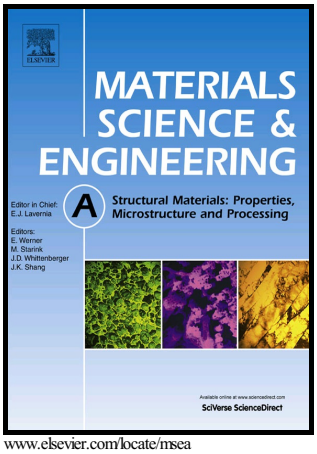

www.elsevier.com/locate/msea

PII: S0921-5093(18)30482-9
DOI: https://doi.org/10.1016/j.msea.2018.03.112
Reference: MSA36305

To appear in: *Materials Science & Engineering A*

Received date: 16 January 2018
Revised date: 27 March 2018
Accepted date: 28 March 2018

Cite this article as: A. Hadadzadeh, F. Mokdad, B. Shalchi Amirkhiz, M.A. Wells, B.W. Williams and D.L. Chen, Bimodal Grain Microstructure Development during Hot Compression of a Cast-Homogenized Mg-Zn-Zr Alloy, *Materials Science & Engineering A,* https://doi.org/10.1016/j.msea.2018.03.112

Bimodal Grain Microstructure Development during Hot Compression of a Cast-Homogenized Mg-Zn-Zr Alloy

A. Hadadzadeh[1*], F. Mokdad[2], B. Shalchi Amirkhiz[3], M.A. Wells[1], B.W. Williams[3], D.L. Chen[2]

[1]Mechanical and Mechatronics Engineering Department, University of Waterloo, 200 University Avenue West, Waterloo, Ontario, N2L 3G1, Canada

[2]Department of Mechanical and Industrial Engineering, Ryerson University, 350 Victoria Street, Toronto, Ontario, M5B 2K3, Canada

[3]CanmetMATERIALS, Natural Resources Canada, 183 Longwood Road South, Hamilton, Ontario, L8P 0A5, Canada

[*]Corresponding author. ahadadza@uwaterloo.ca

Abstract

Hot deformation of a cast-homogenized ZK60 alloy was studied by compression at a temperature of 450°C and a strain rate of $0.001s^{-1}$ to investigate microstructural evolution. The deformed microstructure was characterized using electron backscatter diffraction (EBSD) and high resolution transmission electron microscopy (HRTEM). EBSD observations of the deformed microstructure showed that hot deformation of this alloy resulted in a bimodal grain microstructure consisting of large pancaked unrecrystallized dendrites surrounded by recrystallized equiaxed fine grains. HRTEM studies revealed the presence of nano-(Zn-Zr)-precipitates in the deformed microstructure. Due to the coherency of precipitates/matrix, the

dislocations were pinned by the nano-precipitates inside the unrecrystallized grains and the dislocation motion inside the grains was impeded, hence, a substructure evolved. Consequently, dynamic recrystallization (DRX) was suppressed and deformation was concentrated inside the DRXed region.

Keywords: Magnesium alloy; Dynamic Recrystallization; EBSD; HRTEM; Dislocation.

1. Introduction

Magnesium (Mg) is known to be the lightest structural metallic material. In addition to its low density, other attractive properties of Mg include high specific strength (σ/ρ) and specific stiffness (E/ρ), vibration absorption and good weldability and machinability [1]. As a result, Mg and its alloys are considered as potential replacements for aluminum and steel components in the automotive industry [2, 3]. However, due to its hexagonal crystal structure, Mg has poor formability at low temperatures which makes it mostly used to produce cast and non-critical automotive crash components. Most of the commercial Mg parts are produced using die casting route [3] and only about 10% of Mg components are in the form of wrought products [4]. Since the non-basal slip systems are activated at elevated temperatures [5], wrought magnesium products are fabricated at high temperatures. Moreover, dynamic recrystallization (DRX) is another beneficial microstructural phenomenon occurring at high temperatures [6]. Therefore, expansion of the application of wrought magnesium alloys requires a comprehensive

understanding of high temperature deformation behavior of the alloys along with the effect of deformation parameters and alloying elements on the microstructural evolution.

Wrought Mg alloys mainly contain aluminum (Al), manganese (Mn) and zinc (Zn) as their main alloying elements [7]. Other alloying elements added to the main alloying systems include zirconium (Zr), lithium (Li), tin (Sn) and rare earth (RE) elements [8, 9]. Mg-Zn-Zr alloys have gained attention in the recent years due to their combined high strength and ductility. In this alloy system, Zn is added to improve the strength through solid solution strengthening and Zr acts as a grain refining element which also improves strength [10, 11]. Amongst different variants of this alloy system, ZK60 is the most commonly used [10]. Wrought ZK60 alloys possess the best combination of room temperature strength and ductility among the available wrought Mg alloys [12]. Moreover, this alloy is known to be a suitable alloy for hot deformation and fabrication of wrought products [13-22] where DRX dominates microstructural evolution during hot deformation [23-27]. However, various studies have reported a bimodal grain microstructure consisting of fine recrystallized grains and elongated unrecrystallized ones, which resulted from hot deformation of ZK60 alloy due to partial DRX [25-29]. Shahzad and Wanger [29] reported that the unrecrystallized grains were mainly enriched by Zr. This agrees with the observations made by Oh-ishi et al. [30] where addition of Zr to a Mg-Zn-Ag-Ca alloy led to the formation of a bimodal grain microstructure after hot extrusion of the alloy at 350°C. The authors contributed such a behavior to the suppression of DRX by the fine precipitates inside the grains.

In a recent study, Hadadzadeh et al. [31] observed that even hot deformation of cast-homogenized ZK60 alloy at 450°C resulted in a bimodal grain microstructure. It was observed that the alloy exhibited a rapid DRX at the beginning of hot deformation followed by a near-

saturated DRX kinetics. It was concluded that among the reasons for such a behavior is the rotation of the *c*-axes inside the unrecrystallized grains towards the compression direction during hot deformation, which made these grains unfavorable for further deformation and DRX. The aim of the present study is to better understand the mechanism of DRX and bimodal grain microstructure evolution during hot deformation of cast-homogenized ZK60 alloy by studying the interactions between the dislocations and precipitates, while the previous study [31] mainly focused on texture evolution. Hot compression of a cast-homogenized ZK60 alloy was carried out at 450°C with a strain rate of $0.001s^{-1}$ to a final true strain of 1.0. The deformed microstructure was studied by electron backscatter diffraction (EBSD) and transmission electron microscopy (TEM). The recrystallized and unrecrystallized grains along with the precipitates were analyzed and the resistance of unrecrystallized grains to DRX was discussed.

2. Experimental Procedure

The material used in the current study was a commercially produced as-cast ZK60 with a chemical composition of Mg-5.4wt.%Zn-0.6wt.%Zr. The as-cast billets were received with a billet diameter of 305 mm. The current study was focused on samples taken from a radial position 120 mm away from the center of the billet. Due to incipient melting in the as-cast sample at ~337°C, the alloy was subjected to a homogenization heat treatment at 400°C for 4h, with a slow heating rate. The cast-homogenized ZK60 alloy is called CH-ZK60 hereafter. In order to analyze the precipitates in the alloy, a computational thermodynamics database, FactSage™ with the FTlite database [32] was utilized. Phase identification in the CH-ZK60 alloy was conducted using a PANalytical X-ray diffractometer (XRD) with Cu Kα radiation at 45 kV and 40 mA. The diffraction angle (2θ) ranged between 20° and 110° with a step size of 0.2° and 10 s for each step. Microstructure of the CH-ZK60 alloy was studied using an optical microscope

(OM) and a scanning electron microscope (SEM) JSM-6380LV along with an Oxford energy dispersive X-ray spectroscopy (EDS) system.

Hot deformation of CH-ZK60 alloy was conducted using a Gleeble® 3500 thermal-mechanical simulation testing system to a final true strain of 1.0 at 450°C with a strain rate of $0.001s^{-1}$. Details of these experiments can be found in [31]. The sample was immediately water quenched after compression to preserve the microstructure. The microstructure and microtexture of the deformed sample were studied along the compression axis at the mid-plane position using EBSD. EBSD measurements were performed using an Oxford integrated AZtecHKL advanced EBSD system with NordlysMax2 and AZtecSynergy along with a large area analytical silicon drift detector. The cast-homogenized and deformed microstructure was also studied using an FEI Osiris transmission electron microscope (TEM) equipped with a 200 keV X-FEG gun. The Super-EDS X-ray detection system combined with the high current density electron beam in the scanning mode (STEM) was also utilized to analyze the precipitates. Spatial resolutions in the order of 1 nm were obtained during EDS elemental mapping by using a sub-nanometer electron probe. Electron transparent samples for TEM characterization were prepared by initially cutting a <500 μm thick slice of the sample using a diamond wafering blade followed by punching 3 mm diameter disks with a Gatan puncher and by mechanical polishing of the disks to the thickness of approximately 80-90 μm. Dimpling was done using 4-6 μm CBN paste with a felt wheel and finished using alumina suspension down to about 10 μm at sample center. The final ion milling of the dimpled disk was done using a Gatan 691 PIPS with liquid nitrogen cooling at 5, 3, and 1 keV and gun angle of 4^{o} for 130, 10 and 30 minutes average time at each step respectively, until the perforation.

3. Results

3.1. Microstructure of Cast-Homogenized ZK60

Figure 1 shows the optical microstructure (OM) of CH-ZK60 alloy which consists of dendritic α-Mg resulting from the casting route with an average grain size of ~100 μm, surrounded by interdendritic precipitates. Referring to the isopleth of Mg-0.6wt.%Zr-Zn system predicted by FactSage™ at the Mg-rich corner shown in Figure 2(a), the intermetallic phases formed during solidification of ZK60 alloy are $MgZn_2$ and Zn_2Zr, which were also confirmed by XRD phase identification, as shown in Figure 2(b). The same phases have been observed in ZK60 alloy in previous studies [33, 34]. The predicted amount of $MgZn_2$ during solidification of ZK60 alloy is one order of magnitude higher than Zn_2Zr (~6wt.% versus ~0.6wt.%). Therefore, the dark interdendritic phases observed in the OM of CH-ZK60 alloy are $MgZn_2$ that did not dissolve completely during homogenization heat treatment. Figure 3 illustrates the typical SEM micrograph of the alloy along with one example of EDS analysis of the matrix and intermetallics and an EDS line scan from center to center of two adjacent dendrites. Referring to the Mg-Zr-Zn isopleth, Zr is not soluble in Mg. Therefore, in the intermetallics where Zr is present (Zn_2Zr), Mg amount drops. The Zn_2Zr intermetallics distributed as a discontinuous particles in the microstructure of CH-ZK60 alloy. Moreover, the central region of the dendrites was enriched by Zr, while the amount of Zn was typically higher at the interdendritic regions, referring to Figure 3(b), due to the presence of $MgZn_2$ precipitates.

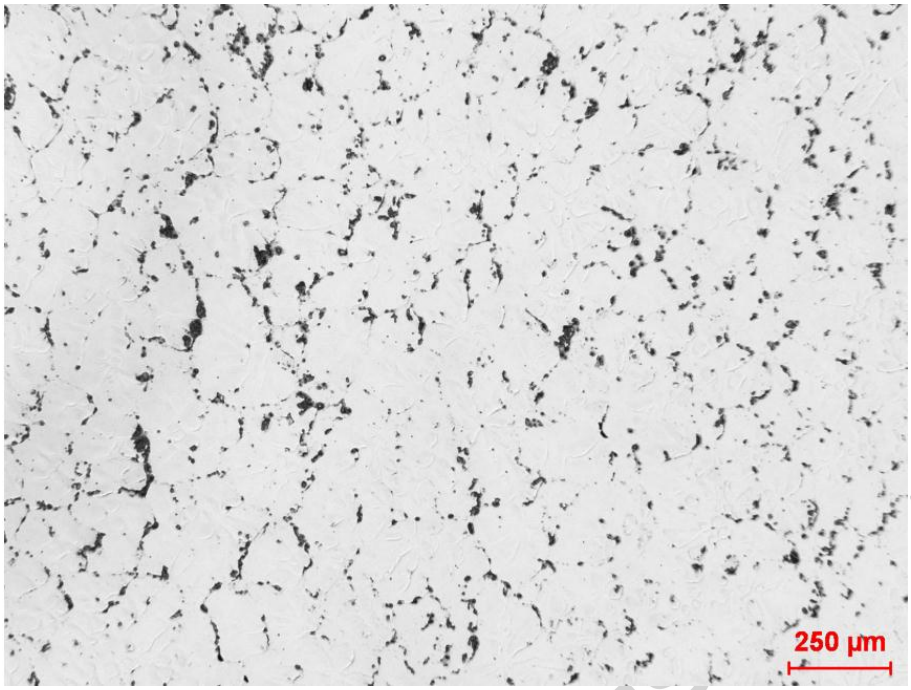

Fig 1- Optical Microstructure of CH-ZK60 alloy.

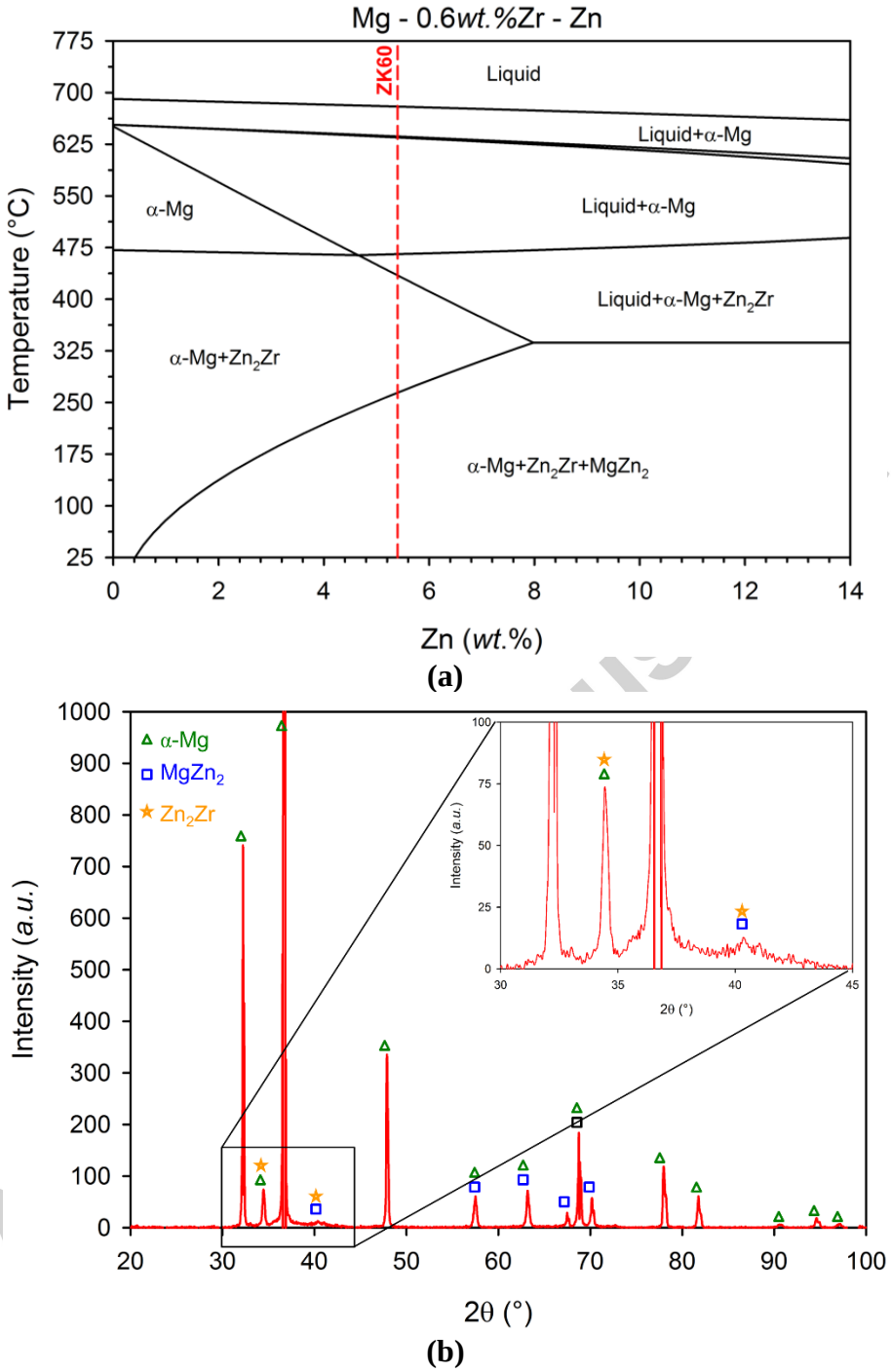

Fig 2- (a) Mg-Zn-Zr isopleth predicted by FactSage™ with 0.6wt.%Zr and (b) XRD diffraction patterns of phases in the CH-ZK60 alloy.

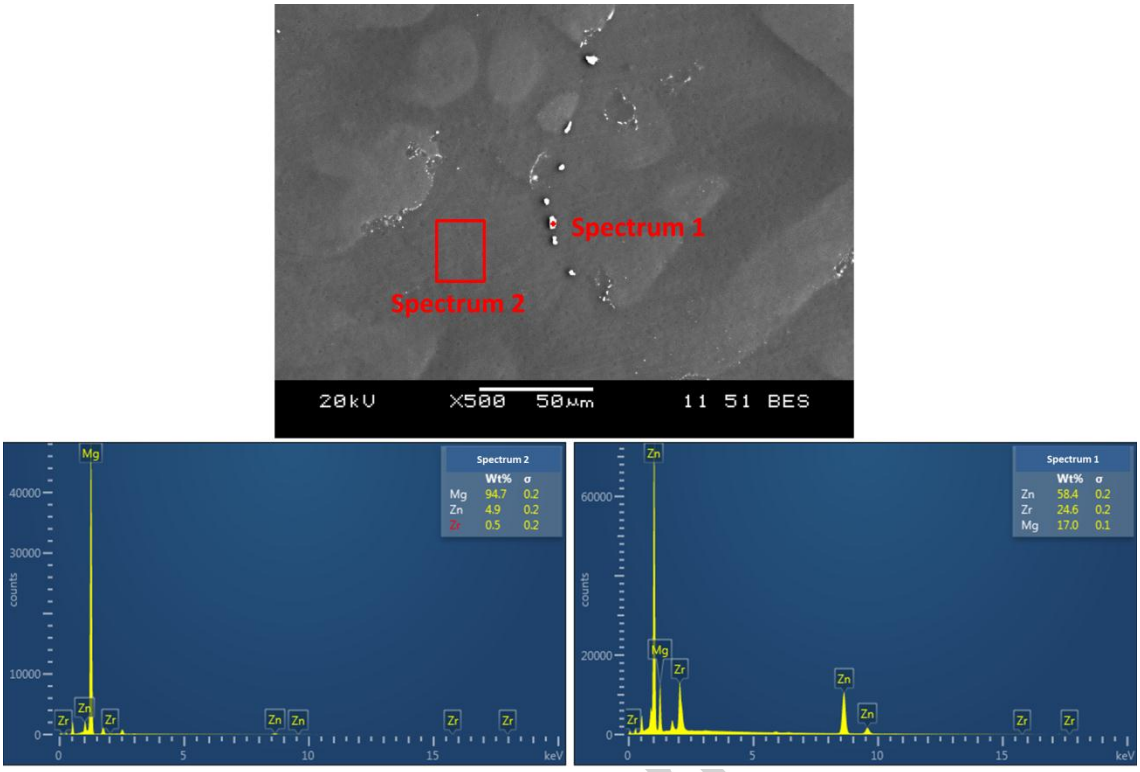
Spectrum 1
Spectrum 2
20kV X500 50µm 11 51 BES
Spectrum 2
Wt% σ
Mg 94.7 0.2
Zn 4.9 0.2
Zr 0.5 0.2
Spectrum 1
Wt% σ
Zn 58.4 0.2
Zr 24.6 0.2
Mg 17.0 0.1
counts
keV

(a)

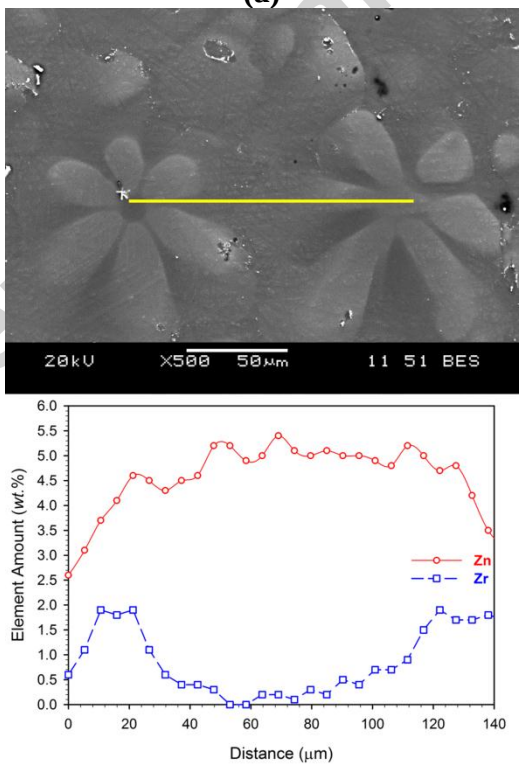
20kV X500 50µm 11 51 BES
Element Amount (wt.%)
Distance (µm)
Zn
Zr

(b)

Fig 3- Typical SEM micrograph of CH-ZK60 with details of (a) EDS analysis of the intermetallic phases and the matrix and (b) EDS line scan between the centers of two adjacent dendrites.

In addition to the micro-size intermetallic phases observed in OM and SEM micrographs, TEM analysis of the microstructure of CH-ZK60 revealed nano-size intermetallic phases. Figure 4 shows the STEM bright field (STEM-BF) image of CH-ZK60 alloy along with STEM-EDS elemental mapping. Homogenization heat treatment of as-cast ZK60 alloy at 400°C led to the formation of rod-shaped nano-precipitates in the microstructure. The EDS mapping of the nano-precipitates, in general, shows depletion of Mg inside the particles, while Zn and Zr were abundant (Figure 4(a)). Figure 4(b) shows details of one particle with a size of ~21 nm. The core of the particle is enriched by Zn and Zr, while by moving toward the edges Zr amount decreases, which is replaced by Mg. In other words, it seems a core-shell type structure exists where the core is Zn_2Zr and the shell is $MgZn_2$. Therefore, both Zn-Zr and Mg-Zn precipitates are found in nano-scale, however the former is significantly higher in amount than the latter.

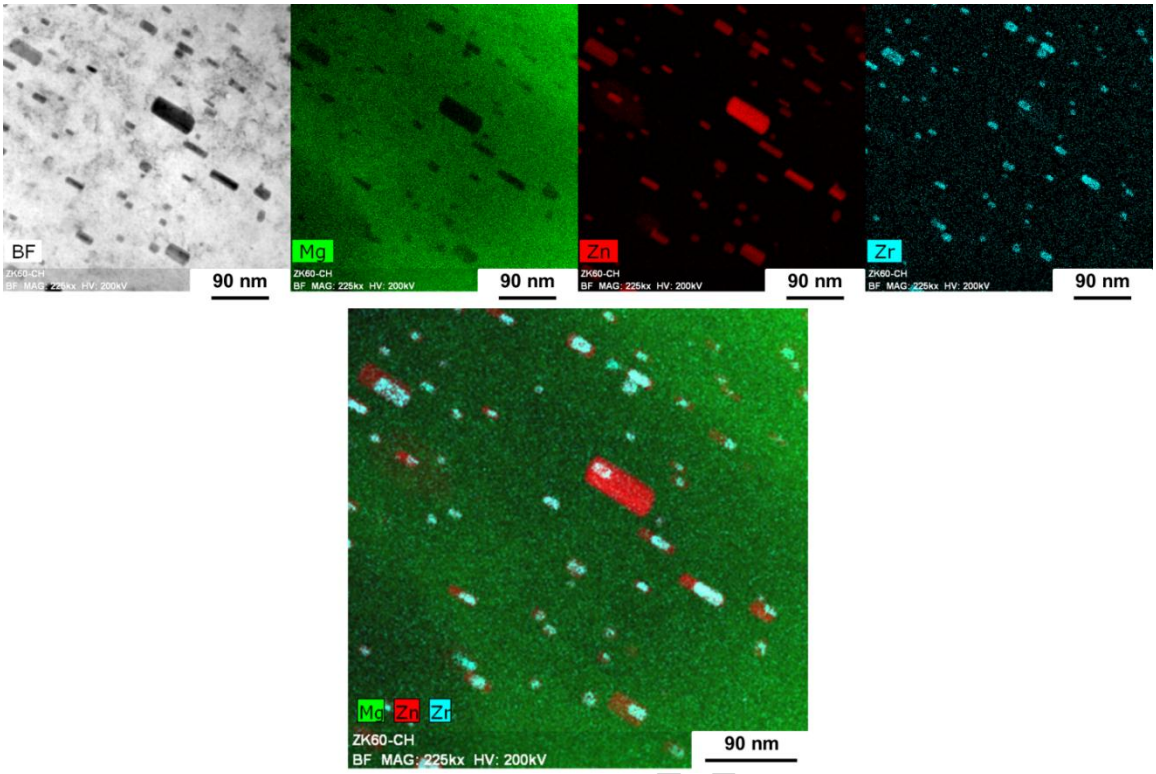
BF
Mg
Zn
Zr
90 nm
ZK60-CH
BF MAG: 225kx HV: 200kV

(a)

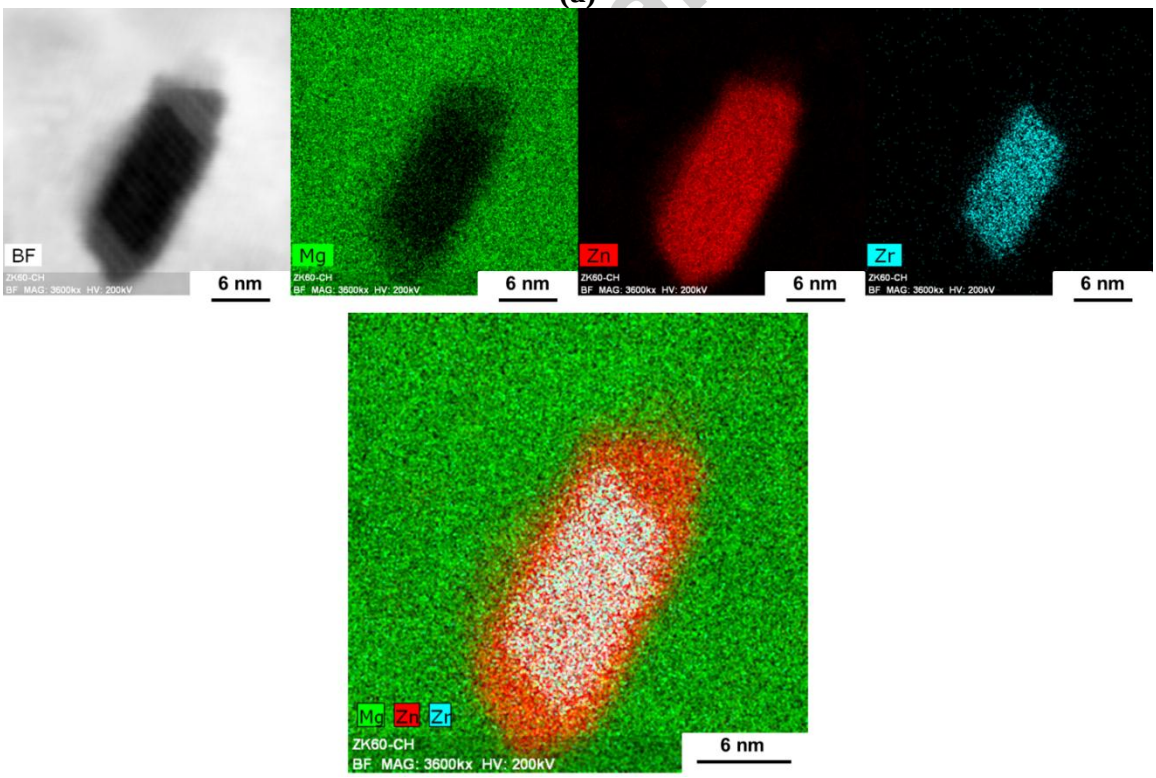
BF
Mg
Zn
Zr
6 nm
ZK60-CH
BF MAG: 3600kx HV: 200kV

(b)

Fig 4- (a) STEM-BF and EDS compositional mapping of CH-ZK60 alloy and (b) details of a nano-size intermetallic phase.

3.2. Microstructure of Deformed CH-ZK60

Figure 5(a) illustrates the inverse pole figure (IPF) map of the deformed CH-ZK60 sample while displaying the grain boundaries (GBs). The microstructure of the deformed CH-ZK60 at 450°C/0.001s^{-1} exhibits a bimodal grain structure consisting of large pancaked unrecrystallized grains (dendrites) surrounded by recrystallized equiaxed fine grains. Such a bimodal microstructure resulting from hot deformation of ZK60 alloy was reported in the previous studies as well [25, 34, 35]. In the IPF map shown in Figure 5(a), high angle grain boundaries (HAGBs) are presented by thick lines and low angle grain boundaries (LAGBs) are shown by thin lines (some of the LAGBs are shown by arrows). As seen, LAGBs have developed significantly inside the unrecrystallized pancaked grains. It was shown in a previous study by Hadadzadeh et al. [31] that during hot deformation of CH-ZK60, DRX initiates from the grain boundaries and proceeds by continuing the deformation. In Figure 5(b), the recrystallized grains were identified based on their grain orientation spread (GOS) value and shown in highlighted color. As seen, there is a significant difference between the recrystallized and unrecrystallized grains in terms of both grain size and aspect ratio. While the average grain size of the recrystallized grains is ~9.8 μm, the length of the unrecrystallized grains can reach about 200-300 μm. The recrystallized fraction of the sample is ~66% (at a final true strain of 1.0).

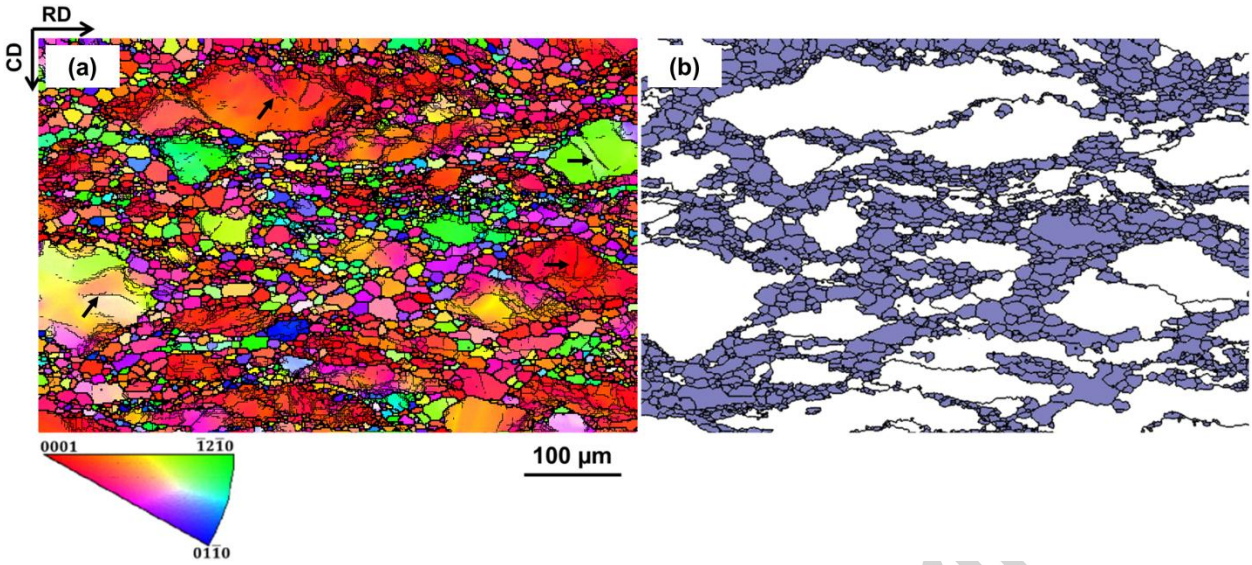

Fig 5- (a) EBSD IPF map of deformed CH-ZK60 at 450°C/0.001s^{-1} and (b) highlighted DRXed grains. HAGBs are shown by thick lines and LAGBs are represented by thin lines in the IPF map (some of the LAGBs are shown by arrows). Note that the IPF color key refers to IPF-Y (along the compression direction). CD represents the compression direction and RD shows the radial direction.

Figure 6 shows the STEM-BF image of typical recrystallized and unrecrystallized grains. The presence of both fine and coarse precipitates in both types of grains is obvious. Similar to the observations from the EBSD map, the development of LAGBs in the unrecrystallized grains is also observed.

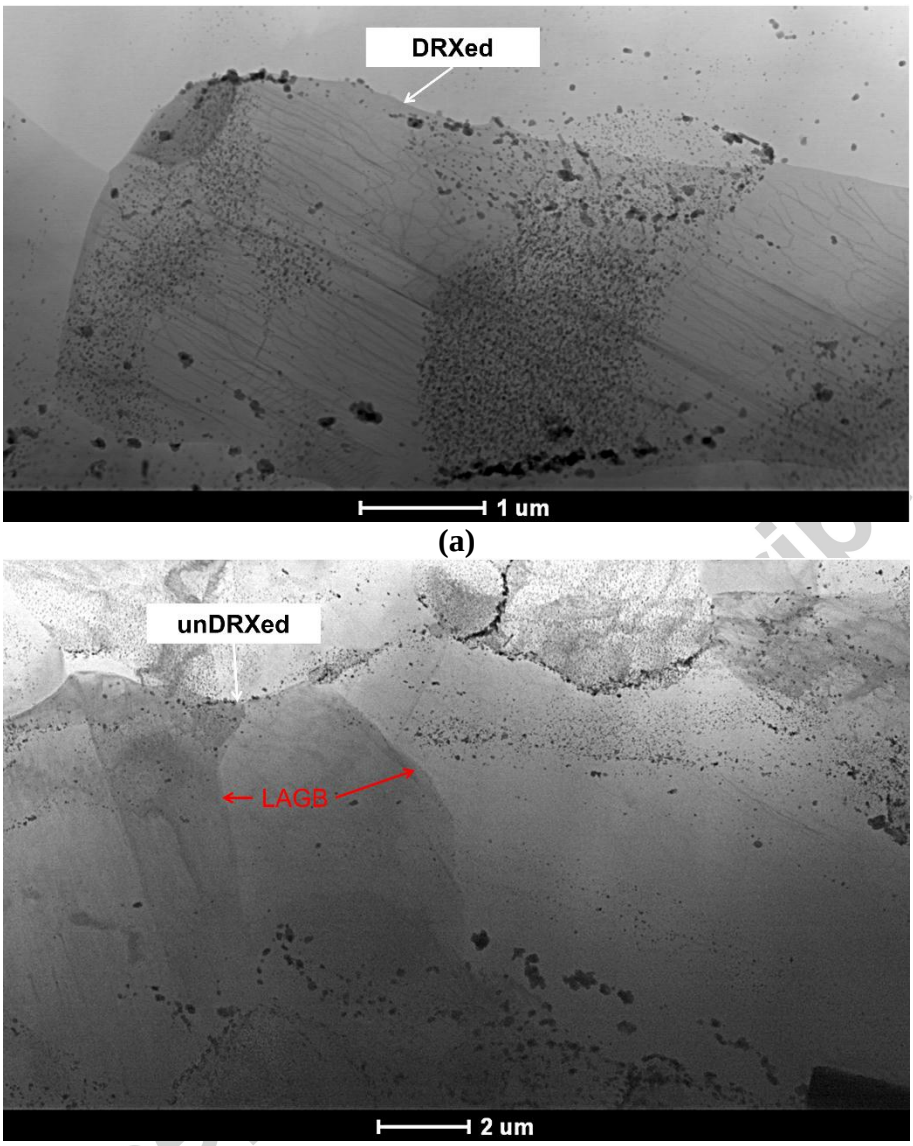

Fig 6- STEM-BF image of a typical (a) DRXed and (b) unDRXed grain.

3.3. Precipitate Characterization of Deformed CH-ZK60

Figure 7 shows STEM high-angle annular dark-filed (HAADF) Z-contrast image, and EDS elemental mapping of deformed CH-ZK60. As seen in Figure 7(a), similar to the homogenized

sample prior to deformation, the precipitates are mainly fine Zn-Zr intermetallics. There are also larger precipitates (shown by red arrays in the HADDF image) where Zn-Zr compounds exist in the core surrounded by a Zn-rich solid solution region. As observed in Figure 7(b), there are locations in the deformed sample where precipitate-free zones (PFZ) formed at the grain boundaries with a width of about 400 nm. It seems that the formation of PFZ is due to depletion of Zr at the grain boundaries, as shown in the EDS line scan in Figure 3(b). Meanwhile, Zn can still be present in the PFZ since in solid solution with Mg. It is also noteworthy to point out the continuous film of Mg-Zn intermetallic formed over the grain boundary in the PFZ, as shown by the red arrows in the HADDF image in Figure 7(b).

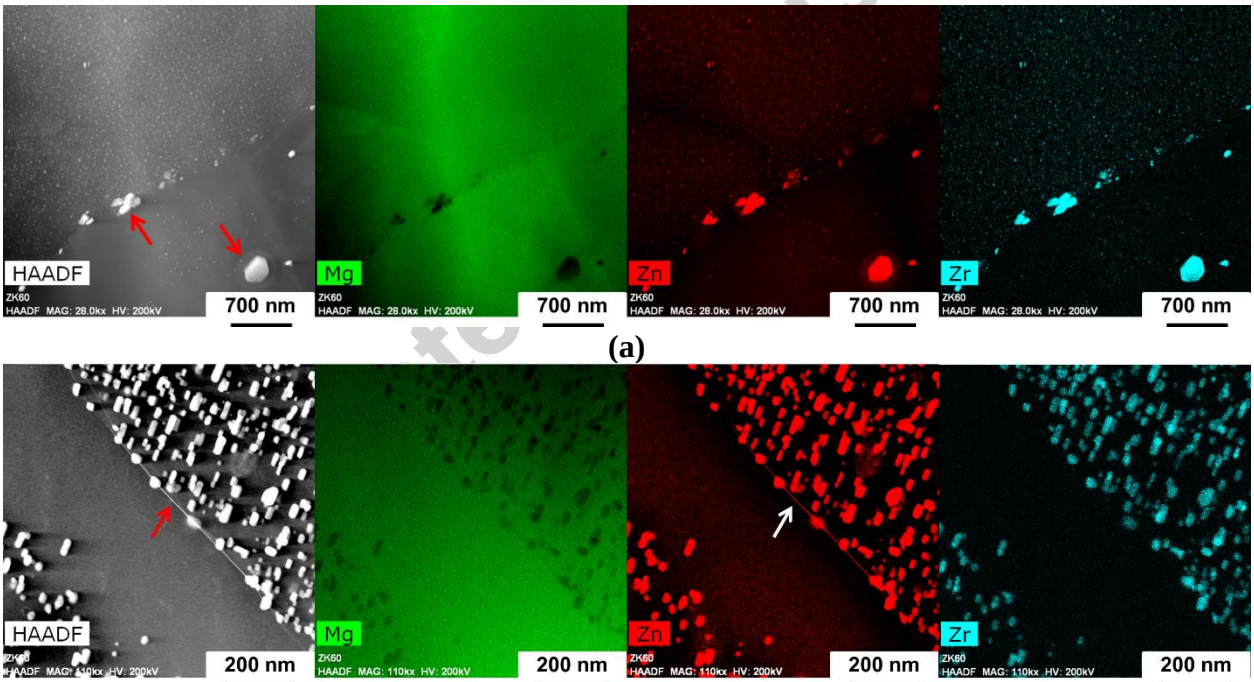

Fig 7- HAADF and EDS compositional mapping of deformed CH-ZK60 (a) typical precipitation behavior and (b) PFZ near a grain boundary.

Figure 8 shows high resolution TEM image of a nano-(Zn-Zr)-precipitate located inside a grain. The precipitate has a rod shape and is coherent with the Mg matrix. Such a behavior of the precipitate is observed as the almost perfect coherency of the atomic planes at the interface of precipitate/Mg matrix.

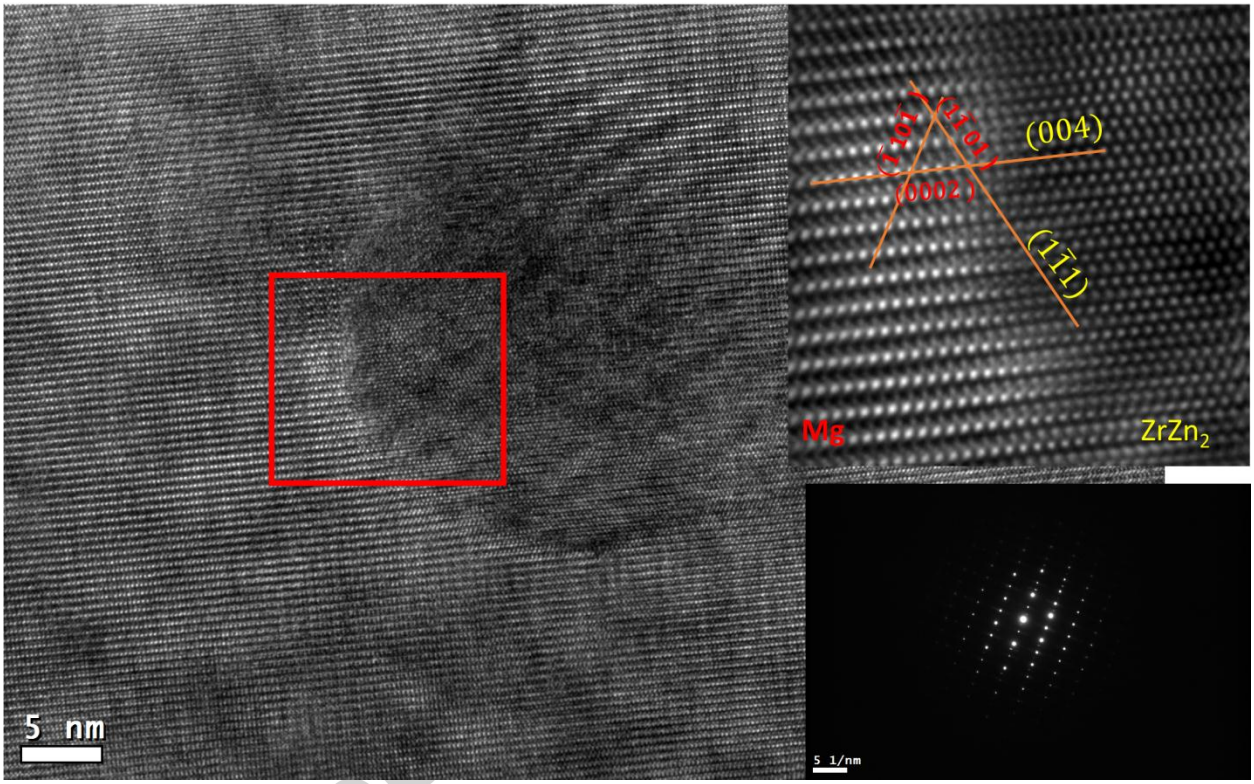

Fig 8- HRTEM micrograph and FFT filtered micrograph on the right showing an almost perfect coherency of the atomic planes at the interface between Mg matrix and $ZrZn_2$ precipitate. SAD pattern from Mg matrix shows $[11\bar{2}0]$ zone axis.

4. Discussion

4.1. Precipitation Behavior in the CH-ZK60 Alloy

Homogenization of as-cast ZK60 at 400°C exposed the alloy above the solvus temperature, where $MgZn_2$ precipitates should dissolve in the α-Mg matrix. However, due to the short time (4h), parts of the $MgZn_2$ precipitates did not dissolve in the matrix. On the other hand, by dissolution of parts of $MgZn_2$ in the matrix, more Zn was available to form Zn-Zr intermetallics at 400°C and the precipitates dispersed as fine particles throughout the microstructure. Since the sample after homogenization was water quenched, the equilibrium cooling condition was not achieved and Zn remained in the Zn-Zr intermetallics and did not form $MgZn_2$ precipitates. Based on the thermodynamics calculations by FactSage™ and previous observations [10], the majority of Zn-Zr intermetallics are in the form of Zn_2Zr.

Due to slow diffusion of Zr in Mg, the core of α-Mg dendrites was enriched by Zr [29, 36], where the amount of this element reached up to ~2wt.% at some points (in comparison with the equilibrium amount of 0.6wt.%), referring to the EDS line scan shown in Figure 3. Hot deformation of a Zr-rich α-Mg will affect the precipitation amount in the core of the dendrites. Figure 9 shows the effect of Zr amount (ranging from 0.6*wt.*% to 2.0*wt.*%) on the Mg-Zn-Zr isopleth, predicted by FactSage™. Increasing the Zr level from 0.6*wt.*% to 2.0*wt.*% increases the solvus temperature (where Zn_2Zr intermetallic precipitates from α-Mg). On the other hand, at the core of the α-Mg where the amount of Zn was less than the equilibrium nominal composition (Figure 3), deformation of CH-ZK60 sample at 450°C occurred in the two-phase regime (α-Mg+Zn_2Zr). Figure 10 shows the predicted effect of Zr content on the amount of Zn_2Zr at 450°C. Since the amount of Zn at the core of the dendrite was less than the equilibrium level, an average

amount of Zn=4.0*wt.*% was assumed to predict the results in Figure 10. As seen, by increasing the Zr amount from 0.6*wt.*% to 2.0*wt.*%, the amount of Zn_2Zr increases from 0.28*wt.*% to 1.5*wt.*% at 450°C. Therefore, Zn_2Zr precipitates play an important role during deformation of Zr rich α-Mg at 450°C in terms of dislocation-precipitate interactions [30], which will be discussed in the coming section.

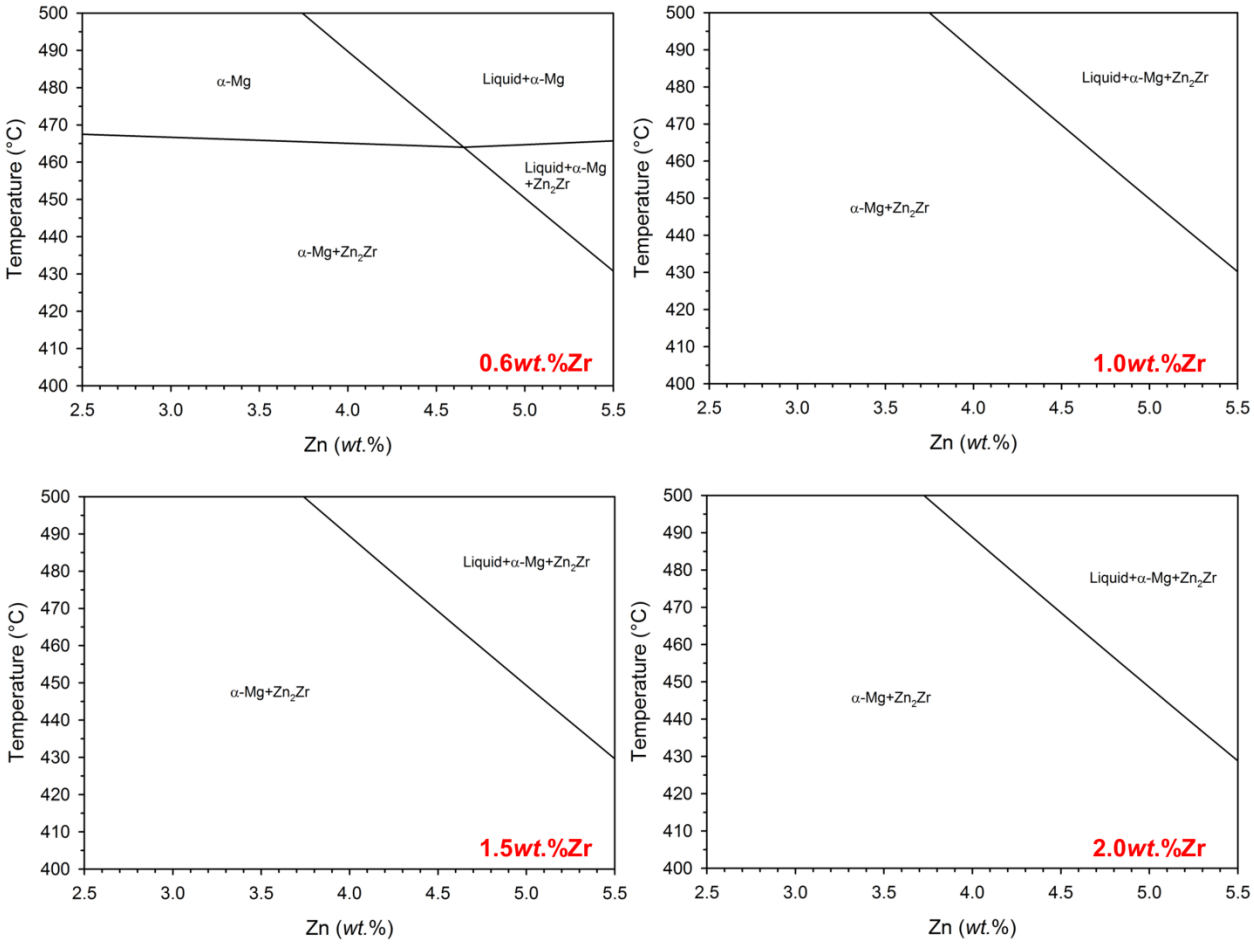

Fig 9- Effect of Zr level on the Mg-Zn-Zr isopleth at the Mg-rich corner.

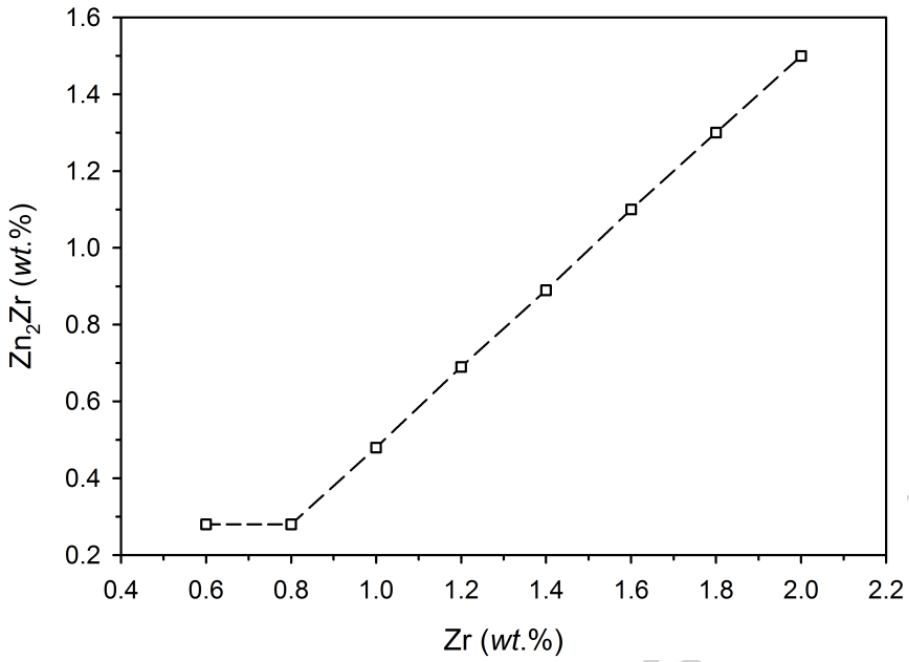

Fig 10- Effect of Zr level on the amount of Zn_2Zr in the Mg-Zn-Zr system at 450°C.

4.2. Interactions between Nano-Precipitates and Dislocations

High resolution STEM BF image of a typical recrystallized grain is shown in Figure 11. Figure 12 shows the similar results for an unrecrystallized grain. As seen in Figure 11, numerous tangled-dislocations are observed inside the DRXed grain, while the dislocations inside the unrecrystallized grain are pinned by the nano-precipitates (Figure 12). The pinning effect of the nano-precipitates is mainly due to coherency of precipitates/matrix [37], as shown in Figure 8. To ensure the maximum dislocation contrast, a multi beam case was adjusted in [0001] zone axis to ensure that $\vec{g}$ vector is not perpendicular to the burgers vector of the dislocations to make them invisible [38]. The density of dislocations was calculated using the procedure reported by Pesicka et al. [39]. To do that, square grid lines were superimposed on the micrograph and number of horizontal and vertical intersections of dislocations with lines (n_h and n_v,

respectively) were counted. In the next step, the total lengths of horizontal lines ($\sum L_h$) and vertical lines ($\sum L_v$) were measured. By knowing the thickness of the sample (t), the dislocation density (ρ_d) was calculated as follows:

$$\rho_d = \frac{1}{t}\left(\frac{\sum n_v}{\sum L_v} + \frac{\sum n_h}{\sum L_h}\right) \quad (1)$$

The thickness of the sample (required for dislocation density measurement) was measured using EELS (electron-energy loss spectroscopy) log ratio technique [40]. The dislocation density inside the DRXed grains was 7.78×10^{13} m^{-2} and inside the unDRXed grains was 2.49×10^{13} m^{-2}. In other words, the density of dislocations inside the recrystallized grains is almost three times higher than that inside the unrecrystallized grains. This is due to the concentration of deformation in the DRXed grains.

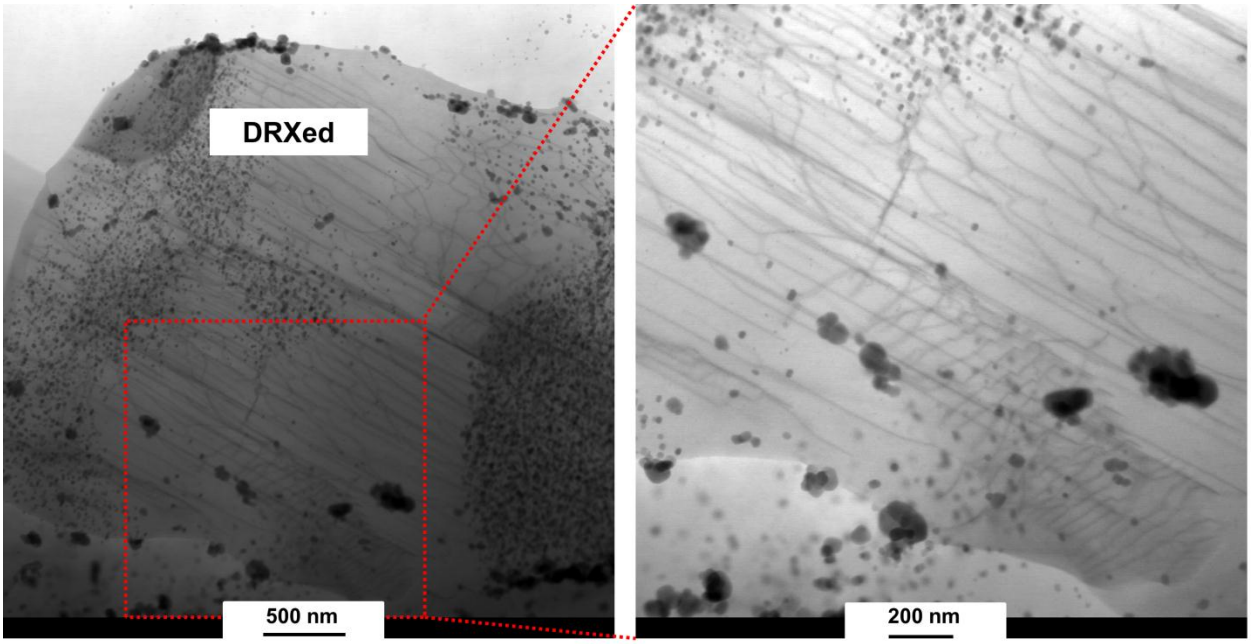

Fig 11- STEM-BF image of a recrystallized grain and details of dislocations network inside the grain.

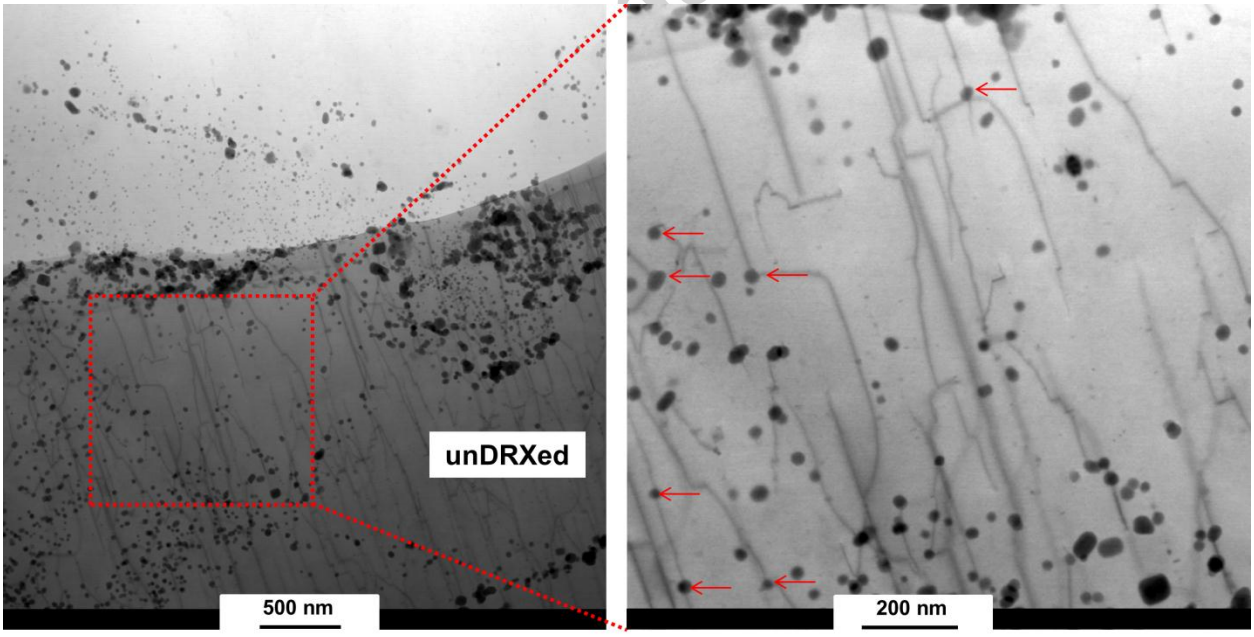

Fig 12- STEM-BF image of an unrecrystallized grain and details of dislocations network inside the grain. The red arrows show the pinned dislocations by the nano-precipitates.

Figure 13 shows the schematic representation of grain structure formation during hot compression of CH-ZK60 alloy. It was shown in a previous study [31] that hot deformation of CH-ZK60 alloy is controlled by discontinuous DRX (DDRX) where the new grains nucleated along the boundaries as a result of bulging of pre-existing HAGBs [41, 42] and leading to the formation of a "necklace-like" grain structure. Bulging of the grain boundaries is caused by the increase of the number of dislocations (as a result of deformation) and dislocation accumulation at the grain boundaries [43]. Formation of new grains by DRX leads to dislocation annihilation and reduction of stored energy. Since DRX is a dynamic process, the formation of new grains requires continuous motion and generation of dislocations to reach the critical point of grain boundary bulging. However, the dislocations inside the unrecrystallized grains were pinned by the nano-precipitates, as shown by the red arrows in Figure 12. As a result of such a pinning effect, the dislocations were not able to move further and new dislocations were not generated. Pinning of dislocations by the precipitates led to evolution of a substructure [30] (LAGBs, as seen in Figure 5(a) and Figure 6(b)) and suppression of DRX inside the unrecrystallized grains. Therefore by continuing the hot compression, deformation of the material concentrated inside the DRXed grains, which resulted in a higher density of dislocations inside these grains. As a result, hot deformation of CH-ZK60 led to evolution of a bimodal grain structure.

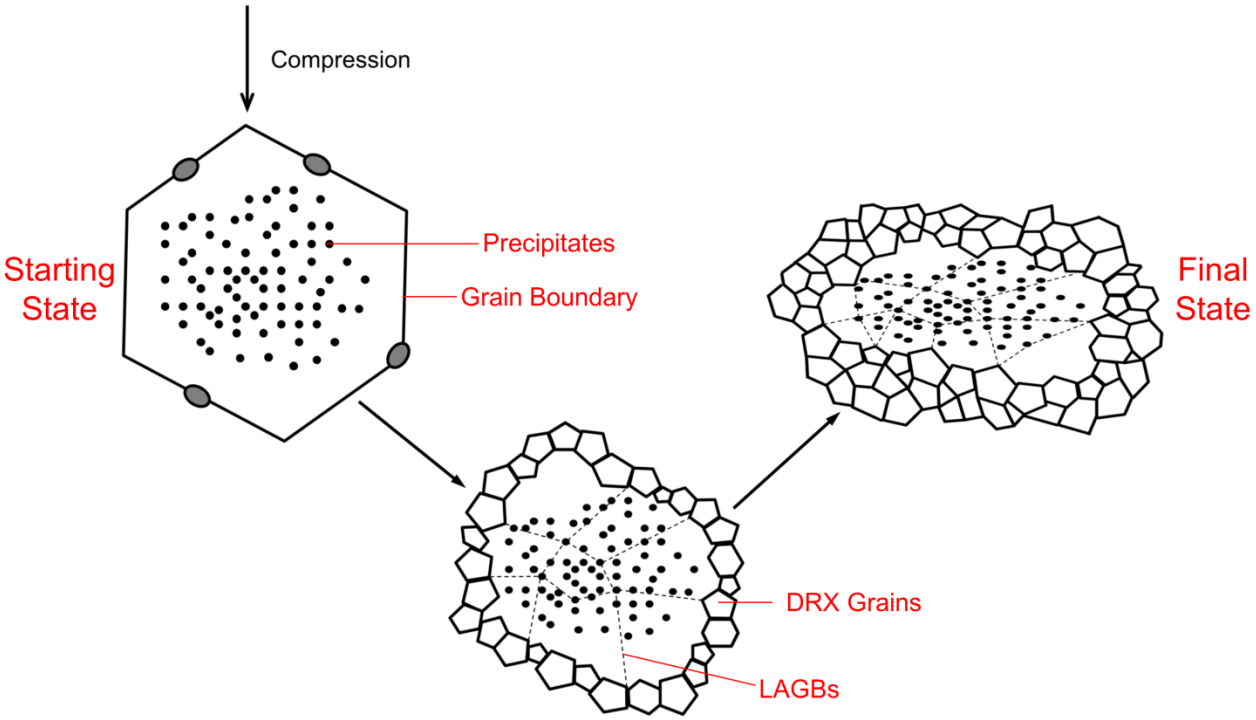

Fig 13- Schematic illustration of the microstructural evolution during hot compression of CH-ZK60 alloy.

Conclusions

In the current study, hot deformation of a cast-homogenized ZK60 alloy was studied at 450°C/0.001s^{-1} to identify the mechanism of evolution of the bimodal grain structure. The material was characterized by SEM, EBSD and TEM to obtain a comprehensive understanding on the mechanism of grain structure development. It was observed that homogenization of as-cast ZK60 alloy at 400°C/4h led to partial dissolution of $MgZn_2$ precipitates, while Zn_2Zr intermetallics presented as nano-precipitates in the microstructure of the alloy. Hot deformation of the alloy resulted in the formation of a bimodal grain microstructure consisting of large pancaked unrecrystallized dendrites surrounded by recrystallized equiaxed fine grains. TEM

observations of the deformed microstructure revealed that the dislocations inside the unrecrystallized grains were pinned by the nano-(Zn-Zr)-precipitates. As a result, the dislocation motion inside the grains was hindered and DRX was suppressed. Therefore by continuing the hot compression, deformation of the material concentrated inside the DRXed grains. Such a heterogeneous deformation was confirmed by the dislocation density inside the recrystallized and unrecrystallized grains. The dislocation density was observed to be about three times higher in the former than in the latter. As a result of such a mechanism, hot deformation of CH-ZK60 led to the evolution of a bimodal grain structure.

Acknowledgements

The authors would like to gratefully acknowledge the financial support of the Natural Sciences and Engineering Research Council of Canada (NSERC), Automotive Partnership Canada (APC) program under APCPJ 459269 - 13 grant with contributions from Multimatic Technical Centre, Ford Motor Company, and Centerline Windsor. The authors would also like to acknowledge Mark Whitney at the University of Waterloo for his help to run the Gleeble machine, Alan Machin and Qinag Li, for the easy access to the laboratory facilities of Ryerson University, and their assistance in XRD phase identification, SEM and EBSD analyses and Renata Zavadil and Catherine Bibby at CanmetMATERIALS for their assistance to facilitate the optical microstructural studies and TEM sample preparation.

References

[1] K.U. Kainer, Magnesium Alloys and Technology, John Wiley & Sons, New York, 2003.

[2] A.A. Luo, Magnesium: current and potential automotive applications, JOM 54 (2) (2002) 42-48.

[3] A.A. Luo, Magnesium casting technology for structural applications, J. Magnes. Alloys 1 (2013) 2-22.

[4] S. You, Y. Huang, K.U. Kainer, N. Hort, Recent research and developments on wrought magnesium alloys, Journal of Magnesium and Alloys (2017), doi: 10.1016/j.jma.2017.09.001.

[5] A. Chapuis, J. Driver, Temperature dependency of slip and twinning in plane strain compressed magnesium single crystals. Acta Mater. 59 (2010) 1986-1994.

[6] R.D. Doherty, D.A. Hughes, F.J. Humphreys, J.J. Jonas, D. Juul Jensen, M.E. Kassner, W.E. King, T.R. McNelley, H.J. McQueen, A.D. Rollett, Current issues in recrystallization: a review, Materials Science and Engineering A 238 (1997) 219–274.

[7] C.J. Bettles, M.A. Gibson, Current Wrought Magnesium Alloys: Strengths and Weaknesses, JOM 57 (2005) 46–49.

[8] H.E. Friedrich, B.L.Mordike, Magnesium Technology-Metallurgy, Design Data, Applications. Springer-Verlag Berlin Heidelberg, 2006.

[9] T.T. Sasaki, K. Yamamoto, T. Honma, S. Kamado, K. Hono, A high-strength Mg–Sn–Zn–Al alloy extruded at low temperature, Scripta Materialia 59 (2008) 1111–1114.

[10] J.D. Robson, C. Paa-Rai, The interaction of grain refinement and ageing in magnesium-zinc-zirconium (ZK) alloys, Acta Mater. 95 (2015) 10-19.

[11] X. Xia, W. Sun, A.A. Luo, D.S. Stone, Precipitation evolution and hardening in Mg-Sm-Zn-Zr alloys, Acta Mater. 111 (2016) 335-347.

[12] D. Orlov, D. Pelliccia, X. Fang, L. Bourgeois, N. Kirby, A.Y. Nikulin, K. Ameyama, Y. Estrin, Particle evolution in Mg-Zn-Zr alloy processed by integrated extrusion and equal channel angular pressing: evaluation by electron microscopy and synchrotron small-angle X-ray scattering, Acta Mater. 72 (2014) 110-124.

[13] F.Fereshteh-Saniee, N.Fakhar, F.Karami, R.Mahmudi, Superior ductility and strength enhancement of ZK60 magnesium sheets processed by a combination of repeated upsetting and forward extrusion, Materials Science & Engineering A 673 (2016) 450–457.

[14] H. Yu, Y. M. Kim, B. S. You, H. S. Yu, S. H. Park, Effects of cerium addition on the microstructure, mechanical properties and hot workability of ZK60 alloy, Materials Science & Engineering A 559 (2013) 798–807.

[15] Y. Yang, L. Jiang, Effect of heat treatment on adiabatic shear susceptibility in ZK60 magnesium alloy, Materials Science & Engineering A 664 (2016) 146–154.

[16] Y. Yuan, A. Ma, X. Gou, J. Jiang, F. Lu, D. Song, Y. Zhu, Superior mechanical properties of ZK60 mg alloy processed by equal channel angular pressing and rolling, Materials Science & Engineering A 630 (2015) 45–50.

[17] X. Chen, F. Pan, J. Mao, J. Wang, D. Zhang, A. Tang, Jian Peng, Effect of heat treatment on strain hardening of ZK60 Mg alloy, Materials and Design 32 (2011) 1526–1530.

[18] Y.D. Yu, C.X. Li, The effect of alternative low frequency electromagnetic field on the solidification microstructure and mechanical properties of ZK60 alloys, Materials and Design 44 (2013) 17–22.

[19] T. Liu, F. Pan, X. Zhang, Effect of Sc addition on the work-hardening behavior of ZK60 magnesium alloy, Materials and Design 43 (2013) 572–577.

[20] L. Liu, X. Chen, F. Pan, A. Tang, X. Wang, J. Liu, S. Gao, Microstructure, texture, mechanical properties and electromagnetic shielding effectiveness of Mg–Zn–Zr–Ce alloys, Materials Science & Engineering A 669 (2016) 259–268.

[21] B. Song, R. Xin, N. Guo, J. Xu, L. Sun, Q. Liu, Dependence of tensile and compressive deformation behavior on aging precipitation in rolled ZK60 alloys, Materials Science & Engineering A 639 (2015) 724–731.

[22] S. Dong, Y. Jiang, J. Dong, F. Wang, W. Ding, Cyclic deformation and fatigue of extruded ZK60 magnesium alloy with aging effects, Materials Science & Engineering A 615 (2014) 262–272.

[23] H.B. He, Q.L. Pan, Q. Chen, Z.Y. Zhang, X.Y. Liu, W.B. Li, Modeling of strain hardening and dynamic recrystallization of ZK60 magnesium alloy during hot deformation, Trans. Nonferr. Met. Soc. China 22 (2012) 246-254.

[24] Y.Q. Yang, B.C. Li, Z.M. Zhang, Flow stress of wrought magnesium alloys during hot compression deformation at medium and high temperatures, Mater. Sci.Eng. A 499 (2009) 238- 241.

[25] C.Y. Wang, X.J. Wang, H. Chang, K. Wu, M.Y. Zheng, Processing maps for hot working of ZK60 magnesium alloy, Mater. Sci. Eng. A 464 (2007) 52-58.

[26] J. Li, J. Liu, Z. Cui, Characterization of hot deformation behavior of extruded ZK60 magnesium alloy using 3D processing maps, Mater. Des. 56 (2014) 889-897.

[27] S.Q. Zhu, H.G. Yan, J.H. Chen, Y.Z. Wu, J.Z. Liu, J. Tian, Effect of twinning and dynamic recrystallization on the high strain rate rolling process, Scr. Mater. 63 (2010) 985–988.

[28] A. Hadadzadeh, M.A. Wells, S.K. Shaha, H. Jahed, B.W. Williams, Role of compression direction on recrystallization behavior and texture evolution during hot deformation of extruded ZK60 magnesium alloy, Journal of Alloys and Compounds 702 (2017) 274-289.

[29] M. Shahzad, L. Wagner, Microstructure development during extrusion in a wrought Mg–Zn–Zr alloy, Scr. Mater. 60 (2009) 536-538.

[30] K. Oh-ishi, C.L. Mendis, T. Homma, S. Kamado, T. Ohkubo, K. Hono, Bimodally grained microstructure development during hot extrusion of Mg–2.4 Zn–0.1 Ag–0.1 Ca–0.16 Zr (at.%) alloys, Acta Materialia 57 (2009) 5593–5604.

[31] A. Hadadzadeh, F. Mokdad, M.A. Wells, D.L. Chen, A New Grain Orientation Spread Approach to Analyze the Dynamic Recrystallization Behavior of a Cast-Homogenized Mg-Zn-Zr Alloy using Electron Backscattered Diffraction, Materials Science & Engineering A 709 (2018) 285-289.

[32] FactSage™, Ver. 6.2. Thermfact (Montreal, Canada) and GTT-Technologies (Aachen, Germany) (1976–2010).

[33] W. Yu, Z. Liu, H. He, N. Cheng, X. Li, Microstructure and mechanical properties of ZK60–Yb magnesium alloys. Mater. Sci. Eng. A 478 (2008) 101–107.

[34] S.M.H. Karparvarfard, S.K. Shaha, S.B. Behravesh, H. Jahed, B.W. Williams, Microstructure, texture and mechanical behavior characterization of hot forged cast ZK60 magnesium alloy. J. Mater. Sci. Technol. 33 (2017) 907–918.

[35] H. Watanabe, K. Moriwaki, T. Mukai, T. Ohsuna, K. Hiraga, K. Higashi, Materials Processing for Structural Stability in a ZK60 Magnesium Alloy. Mater.Trans. 44 (2003) 775–781.

[36] M. Qian, D.H. StJohn, M.T. Frost, Characteristic zirconium-rich coring structures in Mg–Zr alloys. Scr. Mater. 46 (2002) 649–654.

[37] M. Sanjari, A.R. Farkoosh, B. Shalchi Amirkhiz, Y. He, A. Javaid, A.S. Kabir, J. Su, I.H. Jung, S. Yue, The role of the Zn/Nd ratio in the microstructural evolution of the Mg-Zn-Nd system during static recrystallization: Grain boundary partitioning of solutes. Scr. Mater. 134 (2017) 1-5.

[38] D. Rojas, J. Garcia, O. Prat, L. Agudo, C. Carrasco, G. Sauthoff, a. R. Kaysser-Pyzalla, Effect of processing parameters on the evolution of dislocation density and sub-grain size of a 12%Cr heat resistant steel during creep at 650°C, Mater. Sci. Eng. A. 528 (2011) 1372–1381.

[39] J. Pesicka, R. Kuzel, A. Dronhofer, G. Eggeler, The evolution of dislocation density during heat treatment and creep of tempered martensite ferritic steels. Acta Mater. 51 (2003) 4847–4862.

[40] T. Malis, S.C. Cheng, R.F. Egerton, EELS log-ratio technique for specimen-thickness measurement in the TEM., J. Electron Microsc. Tech. 8 (1988) 193–200.

[41] A. Galiyev, R. Kaibyshev, G. Gottstein, Correlation of plastic deformation and dynamic recrystallization in magnesium alloy ZK60, Acta Mater. 49 (2001) 1199-1207.

[42] T. Al-Samman, G. Gottstein, Dynamic recrystallization during high temperature deformation of magnesium, Materials Science and Engineering A 490 (2008) 411–420.

[43] Q. Wang, Y. Chen, M. Liu, J. Lin, H.J. Roven, Microstructure evolution of AZ series magnesium alloys during cyclic extrusion compression. Mater. Sci. Eng. A 527 (2010) 2265–2273.